



Basal and non-basal dislocation slip in Mg–Y

Stefanie Sandlöbes^{a,*}, Martin Friák^b, Jörg Neugebauer^b, Dierk Raabe^a

^a Max-Planck-Institut für Eisenforschung, Department for Microstructure Physics and Alloy Design, Max-Planck-Str. 1, 40237 Düsseldorf, Germany

^b Max-Planck-Institut für Eisenforschung, Department for Computational Materials Design, Max-Planck-Str. 1, 40237 Düsseldorf, Germany

ARTICLE INFO

Article history:

Received 19 December 2012

Accepted 3 March 2013

Available online 21 March 2013

Keywords:

Mg alloys

Mg–Y

Deformation

Dislocations

Transmission electron microscopy

ABSTRACT

The activation of non-basal slip systems is of high importance for the ductility in hcp Mg and its alloys. In particular, for Mg–Y alloys where a higher activation of pyramidal dislocation slip causes an increased ductility detailed characterization of the activated slip systems is essential to understand and describe plasticity in these alloys.

In this study a detailed analysis of the activated dislocations and slip systems via post-mortem TEM and SEM-EBSD based slip band analysis in 3% deformed Mg–3 wt% Y is presented. The analysis reveals a substantial activity of pyramidal $\langle c+a \rangle$ dislocations with different Burgers vectors. The obtained dislocation densities and active slip systems are discussed with respect to atomistic simulations of non-basal dislocations in hcp Mg.

© 2013 Elsevier B.V. All rights reserved.

1. Introduction and motivation

Poor room temperature formability of wrought Mg alloys limits its application in many fields. The combination of strong basal-type texturing and a limited number of available deformation mechanisms is the main reason for the poor room temperature ductility [1].

Y containing Mg alloys exhibit a significantly improved room temperature ductility [2–4] via texture weakening and enhanced activity of non-basal dislocation slip [5]. While in a previous study [6] we analyzed the influence of the alloy-dependent stacking fault energies on the active glide systems in terms of basal and non-basal slip contributions, in the present study we conduct a detailed Burgers vector analysis for a Mg–3 wt% Y model alloy. This analysis is of importance for a fundamental understanding of plasticity in Mg–Y alloys.

The main deformation mechanisms in hexagonal Mg are deformation twinning [e.g. 7–11] and dislocation slip. Besides the primary basal $\langle a \rangle$ slip, additional non-basal dislocation slip is of high importance to fulfill the Taylor criterion for compatible polycrystalline deformation [12]. Despite the high importance for deformation only little is known about the activity and mutual interactions of basal and non-basal dislocations in Mg and Mg alloys. In particular for Mg–Y alloys where a higher activity of pyramidal dislocations is causing up a 5-times higher ductility at room temperature [2–5] validation of theoretical approaches to understand this phenomenon requires detailed characterization of

the activated dislocations. No detailed experimental analysis of dislocation activities in these alloys is published yet.

The aim of this work is to conduct a detailed experimental analysis of active slip systems in a Mg–3 wt% Y alloy. The observations are used to critically evaluate and discuss the predictive capabilities of corresponding atomistic simulations. The work is inspired by the motivation to realize a theory-driven approach to modern alloy design which is based on the joint development of advanced atomistic simulation methods and quantitative microstructural characterization tools that enable the user to scrutinize metallurgical predictions without relying on only simulation or experiment alone.

2. Overview of slip system observations in Mg and Mg alloys

2.1. Activity of slip systems in Mg and Mg alloys in single crystal experiments

Slip band analysis on Mg single crystals [13,14] deformed along the hexagonal axis at temperatures ranging from room temperature to 400 °C showed basal and prismatic slip traces at temperatures below 400 °C. After deformation at 400 °C pyramidal slip traces were observed [13,14]. Another group [15] observed all possible slip systems (basal, prismatic, pyramidal 1 and pyramidal 2) during tensile experiments on single crystals at temperatures between 200 °C and 400 °C. The activation of the different slip systems was found to be dependent on the single crystal orientation in the studied temperature range. Single crystal experiments performed by Hirsch and Lally [16] revealed only dislocations with basal Burgers vector during room temperature deformation.

* Corresponding author. Tel.: +4921 1679 2162; fax: +4921 1679 2333.
E-mail address: s.sandloebes@mpie.de (S. Sandlöbes).

Ando and Tonda [17,18] detected slip lines of the second order pyramidal slip $\{11\bar{2}2\}1/3\langle 11\bar{2}\bar{3}\rangle$ in Mg-Li single crystals by optical microscopy after deformation at 77 K–293 K. The authors observed $\langle c+a \rangle$ screw dislocations and short $\langle c \rangle$ dislocations in MgLi by transmission electron microscopy (TEM). From these observations they concluded that $\langle c+a \rangle$ edge dislocations decompose into sessile $\langle c \rangle$ and mobile $\langle a \rangle$ dislocations while $\langle c+a \rangle$ screw dislocations are mobile.

2.2. Activity of slip systems in Mg and Mg alloys in polycrystal experiments

The observation of second-order $\{11\bar{2}2\}1/3\langle 11\bar{2}\bar{3}\rangle$ pyramidal slip and $\langle c+a \rangle$ dislocations in Mg by TEM was reported by Chino [3], suggesting that only screw $\langle c+a \rangle$ dislocation are stable while edge $\langle c+a \rangle$ dislocations decompose into $\langle a \rangle$ and $\langle c \rangle$ dislocations. Galiyev et al. [19] found $\{11\bar{2}2\}1/3\langle \bar{1}\bar{1}23 \rangle$ slip traces using scanning electron microscopy (SEM) and $\langle c+a \rangle$ dislocations using TEM in warm (423 K) deformed ZK60. They observed increasing $\langle c+a \rangle$ dislocation density with increasing temperature. The authors [19] ascribed the activation of non-basal slip to locally high compatibility stresses at grain boundaries, which exceeds the CRSS for non-basal slip. Agnew et al. [20] performed a TEM study on the dislocation activity in Mg–Li alloys. They found a high density of $\langle c+a \rangle$ dislocations in the Mg–Li alloys, while $\langle c+a \rangle$ dislocations in pure Mg occurred only occasionally in regions with stress concentrations. Koike et al. [21] observed by TEM analysis non-basal cross-slip of $\langle a \rangle$ type dislocations in elongated AZ31, and additionally occasional $\langle c+a \rangle$ dislocations were identified in those grains where the basal planes are oriented parallel to the tensile axis. Chino et al. [3,22] analyzed the deformation behavior of Mg–0.2 wt% Ce, observing an increased room temperature ductility. The authors related this improvement of cold formability to an enhanced activation of non-basal slip, namely prismatic $\langle a \rangle$ slip in the Mg–0.2 wt% Ce alloy [3,22]. Kang et al. [23] revealed the existence of pyramidal dislocations in AZ31 after the sample was processed by ECAP under hydrostatic pressure at 200 °C.

3. Theoretical predictions of slip system activity and structure in Mg and Mg alloys

Molecular dynamics (MD) studies of pyramidal dislocations using Lennard-Jones [24–33] and embedded atom (EAM) [34,35] potentials revealed various stable dislocation core configurations (perfect and dissociated) of pyramidal edge and screw dislocations. Generally, pyramidal screw dislocations were predicted to be both more stable and mobile than edge dislocations.

Li and Ma [36,37] performed molecular dynamics simulations using EAM potentials on pure Mg showing nucleation of partial $\langle c \rangle$ and $\langle a \rangle$ dislocations whose combination then leads to the formation of $\langle c+a \rangle$ dislocations. Corresponding TEM observations [38] of deformed pure Mg also showed dislocations having both $\langle a \rangle$ and $\langle c \rangle$ components.

The existence of stable SFs on pyramidal planes was calculated by MD calculations using Lennard-Jones and EAM potentials [23–34] and the hardsphere-model [39].

Nogaret et al. [40,41] recently presented a MD study by using ab initio-validated EAM potentials on the core structure and motion of pyramidal dislocations between 0 and 300 K. Compared to the earlier studies more stable dislocation core configurations were predicted [40]. Furthermore, some core configurations which were calculated to be stable in earlier studies were found to be not stable [40]. Depending on core type and applied stress dislocation glide on 1st order pyramidal planes or dislocation

dissociation causing either twin nucleation or immobilization were derived. Several stable SF configurations on pyramidal planes were calculated.

Theoretical methods such as MD have the potential to give detailed insights into nucleation, core structure and motion of dislocations in Mg specifically also with respect to effects resulting from rare earth/ Y alloying. However, owing to the variety of the used empirical potentials and the resulting variety in plausibility of the predicted structures and kinetic features of active slip systems atomic-scale predictions should be better interfaced with crisp experimental validation data. The high variety of –partly contradicting– experimental and theoretical data on non-basal dislocations in Mg and Mg alloys shows the necessity of a fundamental investigation of the dislocation activity in Mg alloys.

4. Experimental procedure

Mg–3Y (wt-%, here and below) specimens were produced from 99.98% pure Mg and 99.998% pure Y in a high-pressure induction furnace under a protective gas atmosphere of 20 bar Ar. The as-cast material was homogenized for 20 h at 450 °C and then water-quenched. The annealed slabs were hot-rolled at 500 °C to a total thickness reduction of 50%. Subsequent recrystallization annealing was conducted at 500 °C for 15 min under Ar atmosphere. For TEM observations samples were cold rolled for 3% thickness reduction. TEM observations were performed in a Philips CM20 and a FEG JEOL 2200FS at an acceleration voltage of 200 kV. Thin foils were produced via mechanical grinding followed by electro-polishing until perforation using a twin-jet polisher (Struers TenuPol-5). The electrolyte was a solution of 3 vol% perchloric acid in ethanol. Slip band analysis was performed on electro-polished specimen which were slightly deformed (3%) before observation. Slip band observation was conducted on a JSM6500 JEOL EBSD-SEM.

TEM observations were performed on six different samples which were subjected to the same deformation treatment (3% engineering strain). $\langle c+a \rangle$ dislocations were observed in more than 30 grains (7 different samples) using at least three different two-beam conditions ($g = (0002)$, $g = (11\bar{2}0)$, $g = (11\bar{2}2)$). A complete Burgers vector analysis of the formed dislocation structures was performed in 8 additional grains (6 different samples). This paper presents TEM micrographs of 2 of these samples; in the following referred to as sample I and sample II. The grain orientations of the investigated grains (TEM and SEM-EBSD slip trace analyses) was within $\pm 10^\circ$ basal orientation (basal orientation: (0001)-axis perpendicular to the rolling direction).

5. Experimental Results

Fig. 1 shows the dislocation structure in Mg–3Y after 3% cold rolling. The micrographs show the same area under different diffraction conditions (see inlets for diffraction vector g). Both, bright field and weak-beam dark field (WBDF) images of the respective diffraction conditions are presented. According to the $g \cdot b$ criterion (b : Burgers vector) dislocations with different Burgers vectors are visible when $g \cdot b \neq 0$ and invisible when $g \cdot b = 0$. Actually, small values of $g \cdot b (< 0.5)$ are difficult to be distinguished from $g \cdot b = 0$.

The $g \cdot b$ values for the diffraction conditions presented in Figs. 1, 3 and 4 are summarized in Table 1.

The analysis reveals that $\langle c+a \rangle$ dislocations of different Burgers vectors are present, namely, $b = 1/3[11\bar{2}3]$, $b = 1/3[11\bar{2}\bar{3}]$ and $b = 1/3[211\bar{3}]$. Additionally, the collinear dissociation of $b = 1/3[11\bar{2}3]$ dislocations according to $1/3[11\bar{2}3] \rightarrow 1/6[20\bar{2}3] + 1/6[0\bar{2}\bar{2}3]$ is observed. The corresponding dissociation width amounts

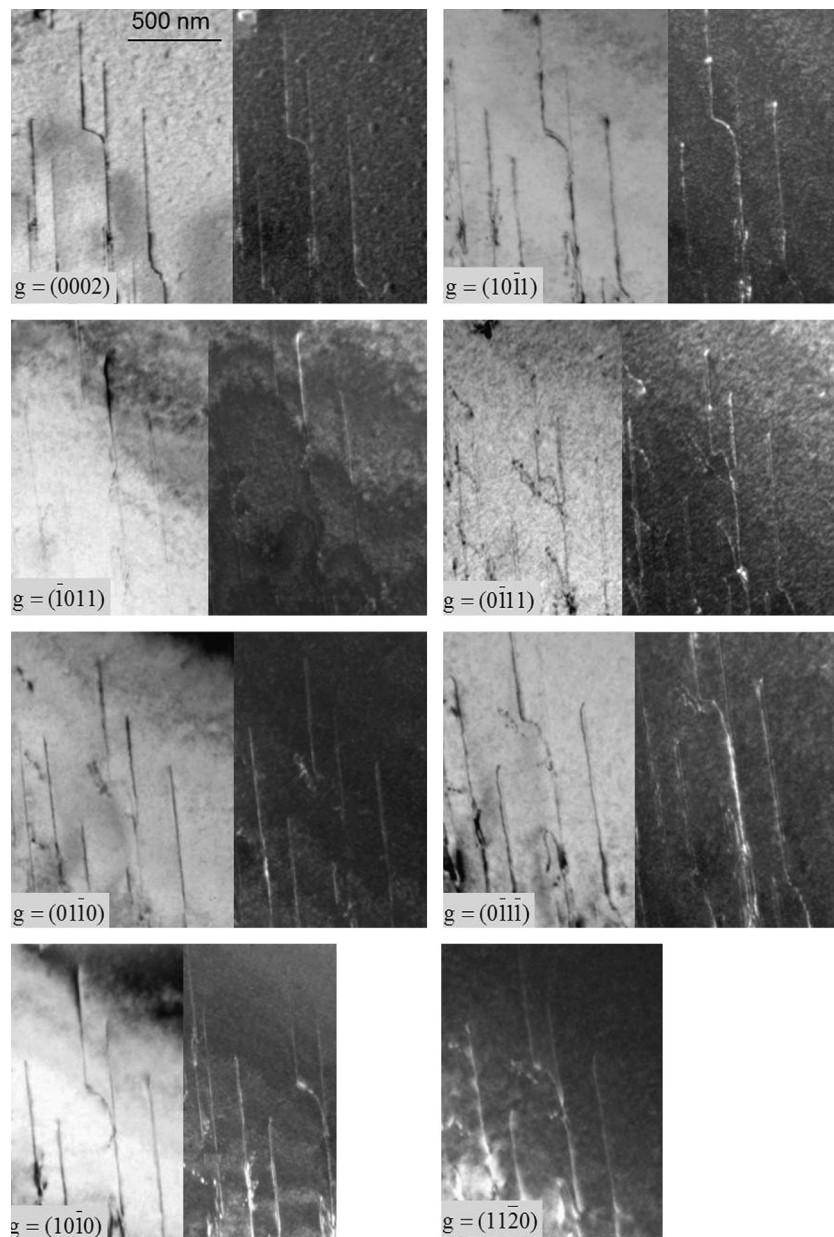


Fig. 1. Bright field and weak-beam dark field images of the dislocation structure in Mg-3Y after 3% cold rolling in sample I. Each micrograph shows the same area under different diffraction conditions (see inset for diffraction vector g). The sequential use of different diffraction conditions is required to identify the Burgers vectors of dislocations.

to a value below 5 nm after 3% deformation (engineering strain). Besides these pyramidal dislocations basal dislocations with a Burgers vector $b = 1/3[1\bar{2}10]$ and the basal intrinsic stacking fault I_2 (SF_2 $1/3[11\bar{2}0] \rightarrow 1/3[10\bar{1}0] + 1/3[01\bar{1}0]$) are observed.

A schematic figure of the dislocation configuration is presented in Fig. 2.

Figs. 3 and 4 show another specimen subjected to the same deformation treatment, sample II. Here larger portions of a grain were selected and consequently the Burgers vector analysis was conducted for more complex dislocation arrangements and not only for single dislocations. This is important in order to also visualize possible reaction products or dislocation configurations that result from cross slip events that can occur when dislocations interact. In sample II (Figs. 3 and 4), both, basal $\langle a \rangle$ and pyramidal $\langle c+a \rangle$ dislocations are observed. Dislocations which are invisible under $g = (0002)$ are basal $\langle a \rangle$ dislocation having Burgers vectors $b = 1/3[11\bar{2}0]$ and $b = 1/3[1\bar{2}10]$ (denoted A in Figs. 3 and 4).

Those dislocations which are visible under $g = (0002)$, $g = (10\bar{1}0)$, $g = (10\bar{1}1)$, $g = (0\bar{1}\bar{1}\bar{1})$ and $g = (0\bar{1}\bar{1}0)$ and invisible under $g = (\bar{1}011)$ and $g = (0\bar{1}11)$ have a Burgers vector $b = 1/3[11\bar{2}3]$ (denoted B in Figs. 3 and 4). Another group of pyramidal dislocations was observed, they have the Burgers vector $b = 1/3[11\bar{2}\bar{3}]$ (denoted C in Figs. 3 and 4). According to the $g \cdot b$ criterion these dislocations are visible under $g = (0002)$, $g = (\bar{1}011)$, $g = (10\bar{1}0)$, $g = (0\bar{1}11)$ and $g = (0\bar{1}\bar{1}0)$ and invisible at $g = (10\bar{1}1)$, $g = (0\bar{1}\bar{1}\bar{1})$. As already presented for sample I a third group of pyramidal dislocations is found in sample II. As these dislocations are visible under $g = (0002)$, $g = (10\bar{1}0)$, $g = (10\bar{1}1)$, $g = (0\bar{1}\bar{1}\bar{1})$ and $g = (0\bar{1}\bar{1}1)$ and invisible under $g = (\bar{1}011)$ and $g = (0\bar{1}\bar{1}0)$ their Burgers vector is $b = 1/3[2\bar{1}1\bar{3}]$ (denoted D in Figs. 3 and 4). The label F in Figs. 3 and 4 marks collinearly dissociated pyramidal dislocations $1/3[2\bar{1}1\bar{3}] \rightarrow 1/6[20\bar{2}\bar{3}] + 1/6[2\bar{2}0\bar{3}]$ (labeled F in Figs. 3 and 4).

For better clarity of the images, the labeling of each different dislocation group is only inserted in one of the micrographs.

Table 1
Calculated $g \cdot b$ values for the diffraction conditions used to image the dislocations in samples I-III.

Burgers vector b	Diffraction vector g										
	0002	-1011	10-10	11-20	10-11	0-11-1	0-111	01-10	10-1-1	01-11	-1010
perfect $\frac{1}{3}[11-20]$	0.00	-1.00	1.00	2.00	1.00	-1.00	-1.00	1.00	1.00	1.00	-1.00
perfect $\frac{1}{3}[1-210]$	0.00	0.00	0.00	-1.00	0.00	1.00	1.00	-1.00	0.00	-1.00	0.00
perfect $\frac{1}{3}[-2110]$	0.00	1.00	-1.00	-1.00	-1.00	0.00	0.00	0.00	-1.00	0.00	1.00
perfect [0001]	2.00	1.00	0.00	0.00	1.00	-1.00	1.00	0.00	-1.00	1.00	0.00
perfect $\frac{1}{3}[3,11-22]$	2.00	0.00	1.00	2.00	2.00	-2.00	0.00	1.00	0.00	2.00	-1.00
perfect $\frac{1}{3}[1-213]$	2.00	1.00	0.00	-1.00	1.00	0.00	2.00	-1.00	-1.00	0.00	0.00
perfect $\frac{1}{3}[-2113]$	2.00	2.00	-1.00	-1.00	0.00	-1.00	1.00	0.00	-2.00	1.00	1.00
perfect $\frac{1}{3}[11-2-3]$	-2.00	-2.00	1.00	2.00	0.00	0.00	-2.00	1.00	2.00	0.00	-1.00
perfect $\frac{1}{3}[1-21-3]$	-2.00	-1.00	0.00	-1.00	-1.00	2.00	0.00	-1.00	1.00	-2.00	0.00
perfect $\frac{1}{3}[-211-3]$	-2.00	0.00	-1.00	-1.00	-2.00	1.00	-1.00	0.00	0.00	-1.00	1.00
partial $\frac{1}{3}[10-10]$	0.00	-0.67	0.67	1.00	0.67	-0.33	-0.33	0.33	0.67	0.33	-0.67
partial $\frac{1}{3}[1-100]$	0.00	-0.33	0.33	0.00	0.33	0.33	0.33	-0.33	0.33	-0.33	-0.33
partial $\frac{1}{3}[01-10]$	0.00	-0.33	0.33	1.00	0.33	-0.67	-0.67	0.67	0.33	0.67	-0.33
partial $\frac{1}{2}[0001]$	1.00	0.50	0.00	0.00	0.50	-0.50	0.50	0.00	-0.50	0.50	0.00
partial $\frac{1}{6}[3,20-22]$	1.00	-0.17	0.67	1.00	1.17	-0.83	0.17	0.33	0.17	0.83	-0.67
partial $\frac{1}{6}[2-20-3]$	-1.00	-0.83	0.33	0.00	-0.17	0.83	-0.17	-0.33	0.83	-0.83	-0.33
partial $\frac{1}{6}[02-2-3]$	-1.00	-0.83	0.33	1.00	-0.17	-0.17	-1.17	0.67	0.83	0.17	-0.33
partial $\frac{1}{6}[-2023]$	1.00	1.17	-0.67	1.00	-0.17	-0.17	0.83	-0.33	-1.17	0.17	0.67
partial $\frac{1}{6}[02-23]$	1.00	0.17	0.33	1.00	0.83	-1.17	-0.17	0.67	-0.17	1.17	-0.33
partial $\frac{1}{6}[20-2-3]$	-1.00	-1.17	0.67	1.00	0.17	0.17	-0.83	0.33	1.17	-0.17	-0.67
partial $\frac{1}{6}[11-21]$	0.33	-0.33	0.50	1.00	0.67	-0.67	-0.33	0.50	0.33	0.67	-0.50
partial $\frac{1}{6}[11-2-1]$	-0.33	-0.67	0.50	1.00	0.33	-0.33	-0.67	0.50	0.67	0.33	-0.50

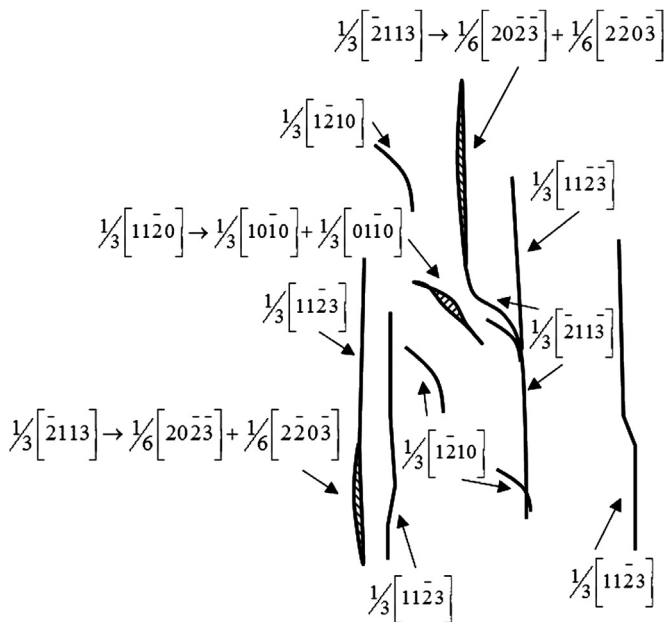


Fig. 2. Schematic drawing of the dislocation configuration in sample I.

6. Discussion

Post-mortem TEM analysis of activity and interaction of dislocations in Mg-3Y reveals a significant activity (about 65%) and interaction of pyramidal dislocations during the early stages of plastic deformation (3% engineering strain) at room temperature. Table 2 gives an overview of the frequency of the observed basal and non-basal dislocations, both in perfect and dissociated states.

Generally, it is difficult in such an approach to differentiate between geometrically necessary dislocations (GND) and statistically stored dislocations (SSD) in a post-mortem analysis. Because of this conceptual problem and due to the fact that a very limited number of experimental studies on dislocation activities in hcp Mg exist we conducted a slip trace analysis using SEM-EBSD on Mg-3Y. The rationale behind combining an EBSD based slip trace

analysis with direct TEM observations of individual dislocations is that this approach allows us to observe the active glide planes of the dislocations during plastic deformation by EBSD-SEM and the associated $\langle a \rangle$ or $\langle c+a \rangle$ Burgers vectors by TEM. The combination of these two methods is necessary to identify the types, Burgers vectors and glide planes of the active dislocations during plastic deformation. Fig. 5 shows the results of the conducted slip-trace analysis.

As shown in Fig. 5 slip bands on three different glide planes were observed: basal plane (0001), 1st order pyramidal plane ($10\bar{1}1$) and 2nd order pyramidal plane ($11\bar{2}2$). The slip band densities range from approximately 70% basal plane slip traces and 30% pyramidal plane slip traces (Fig. 5 left image) to approximately 60% basal plane slip traces and 40% pyramidal plane slip traces (Fig. 5 right image). The wavy appearance of the pyramidal plane slip bands is due to cross-slip of the dislocations indicating that they are formed by non-basal dislocations [3]. This is supported by the post-mortem TEM analysis where we found no pyramidal $\langle a \rangle$ slip. The quantitative differences and scatter in the densities of basal and pyramidal dislocations observed between the post-mortem TEM analysis on the one hand and the slip band analysis in SEM-EBSD on the other hand might be due to one or more of the following reasons:

- the post-mortem SSD density of basal $\langle a \rangle$ dislocations is probably lower compared to pyramidal $\langle c+a \rangle$ dislocations because of defined slip bands and easy glide of basal $\langle a \rangle$ dislocations;
- basal $\langle a \rangle$ dislocations might form higher surface steps than pyramidal $\langle c+a \rangle$ dislocations as they (basal $\langle a \rangle$) glide only along the defined basal slip band. Pyramidal dislocations glide on several planes and, hence, do not form such defined surface steps (see also the wavy appearance of pyramidal plane slip bands in Fig. 5);
- pyramidal dislocations interact and can form networks, consequently, not all pyramidal dislocations reach the surface.

By using the software TOCA [41,42] we determined that most of the observed perfect pyramidal dislocations were screw dislocations on the 1st order (higher density) and 2nd order pyramidal planes.

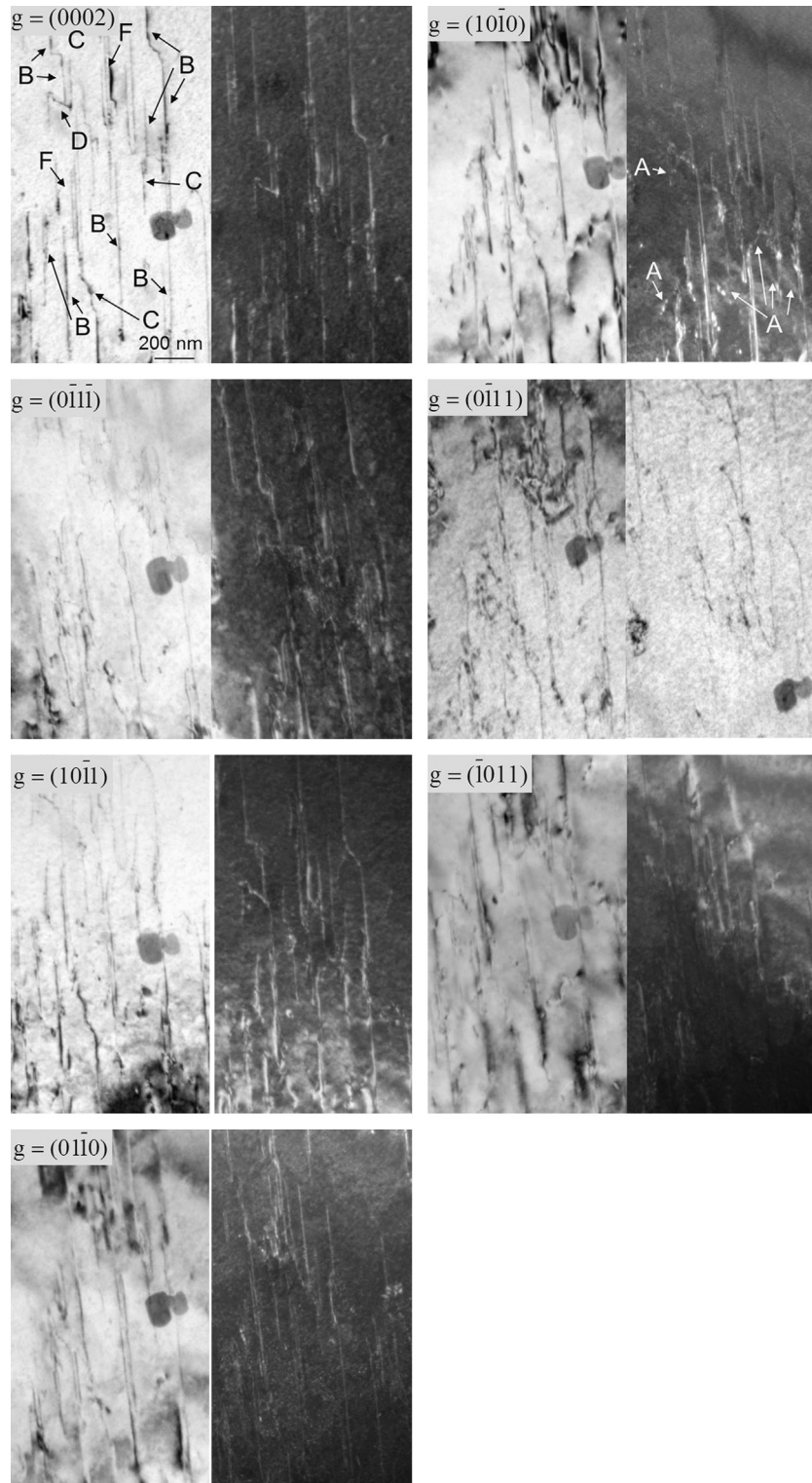


Fig. 3. Bright field and weak-beam dark field images of the dislocation structure in Mg-3Y after 3% cold rolling in sample II (region1), each micrograph shows the same area under different diffraction conditions (see inlet for diffraction vector g). The sequential use of different diffraction conditions is required in order to make all dislocations visible.

This confirms the predictions of various MD studies [24–35,40] showing higher stability and mobility of pyramidal screw dislocations as compared to the properties of the pyramidal edge dislocations. While these theoretical studies found pyramidal screw dislocations only on the 1st order pyramidal planes, we observed pyramidal dislocations on 1st and also on 2nd order pyramidal

planes. The wavy appearance of the observed pyramidal dislocations in the TEM analysis indicates frequent cross-slip allowing dislocations to move from one pyramidal plane to another and, by that, promoting homogeneous and compatible deformation. This discrepancy between MD based predictions and our current experimental findings might be caused by the empirical potentials implemented

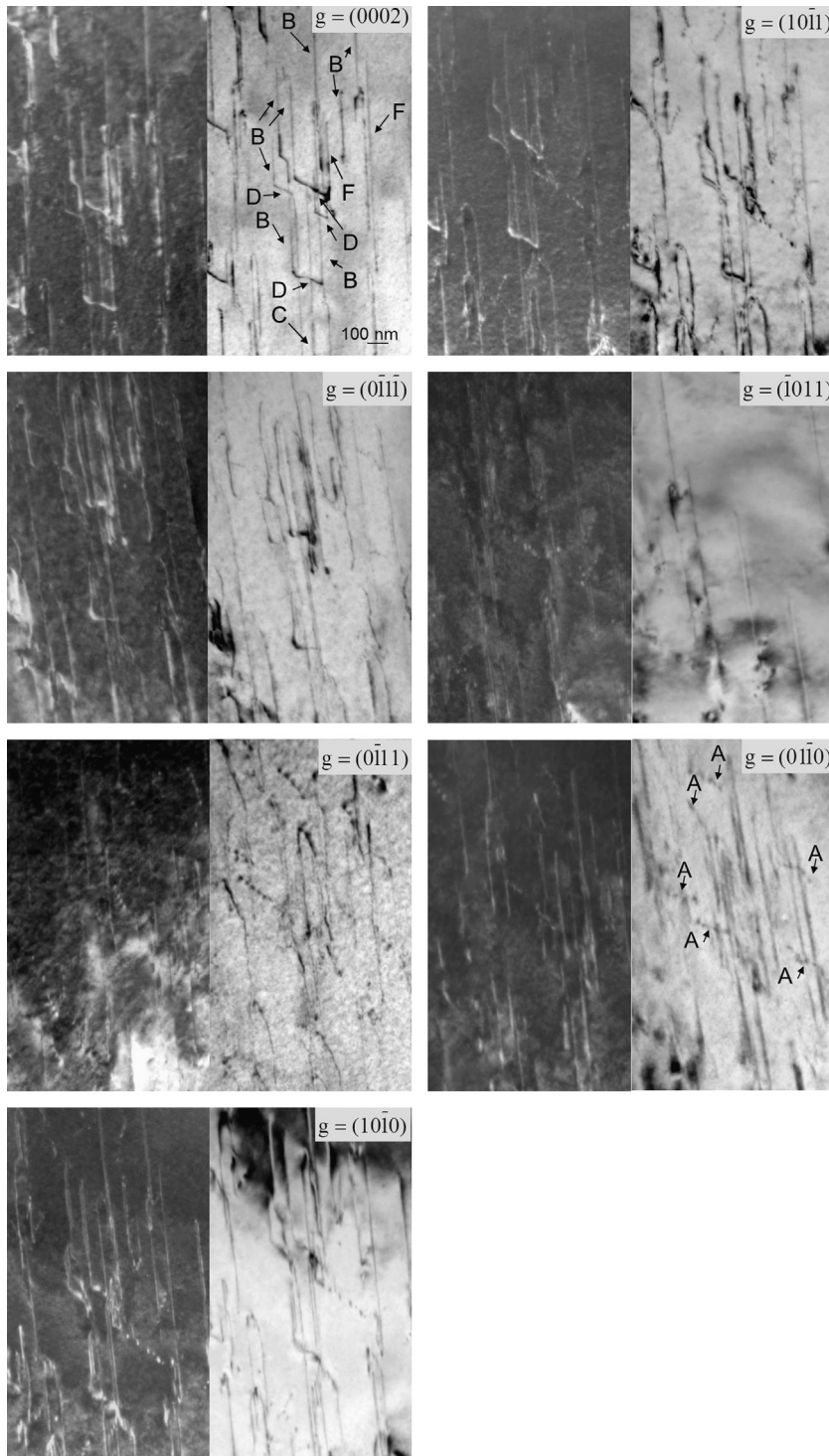


Fig. 4. Bright field and weak-beam dark field images of the dislocation structure in Mg-3Y after 3% cold rolling in sample II (region 2), each micrograph shows the same area under different diffraction conditions (see inset for diffraction vector g). The sequential use of different diffraction conditions is required in order to make all dislocations visible.

for most of the MD calculations in combination with the complex structure of the pyramidal planes in hcp structures.

All published MD studies reveal the existence of stable SFs on pyramidal planes by dissociation of perfect $\langle c+a \rangle$ dislocations [24–35,39,40]. The glide of $\langle c+a \rangle \rightarrow 1/2\langle c+a \rangle + 1/2\langle c+a \rangle$ dissociated screw dislocations with a dissociation widths of a few times the lattice parameter a was proposed [28–33].

Experimentally we observed collinearly dissociated $\langle c+a \rangle$ dislocations according to:

$$1/3[11\bar{2}3] \rightarrow 1/6[20\bar{2}3] + 1/6[02\bar{2}3] \text{ and}$$

$$1/3[\bar{2}113] \rightarrow 1/6[20\bar{2}3] + 1/6[2\bar{2}03]$$

The observed dissociation widths of the partial dislocations are below 5 nm. As the dissociation occurred in the glide plane, the dissociated dislocations may be mobile as long as the dissociation width is small enough.

Prismatic $\langle a \rangle$ slip was not observed in the present study. Probably, the required shear stress for cross-slip of basal dislocations onto prismatic planes becomes more prevalent at higher strains as suggested by some earlier works [3,22].

Table 2

Frequency of dislocations observed in samples I–II (Figs. 1, 3 and 4) and samples III–VI (not shown in this paper) via post-mortem TEM analysis. The analysis is based on complete Burgers vector analyses in 8 grains.

Dislocation type	Dislocation Burgers vector	Amount (%)	Amount (%)
Basal	perfect $b = 1/3[11\bar{2}0]$ and $b = 1/3[1\bar{2}10]$	35	32.5
	dissociated ($SF_1 + SF_2$) $b = 1/3[1\bar{2}10]$		2.5
Pyramidal	perfect $b = 1/3[11\bar{2}3]$ screw	65	31.5
	perfect $b = 1/3[11\bar{2}\bar{3}]$ screw		8
	perfect $b = 1/3[2\bar{1}1\bar{3}]$ mixed		18.5
	dissociated		
	$1/3[11\bar{2}3] \rightarrow 1/6[20\bar{2}3] + 1/6[02\bar{2}3]$ and $1/3[2\bar{1}1\bar{3}] \rightarrow 1/6[20\bar{2}3] + 1/6[2\bar{2}0\bar{3}]$		7

With the presented experimental dislocation analysis we hence aim at providing quantitative experimental data that can be used for validation of theoretical results to obtain an improved fundamental understanding of dislocation-driven plasticity phenomena in Mg–Y alloys.

7. Conclusions

The remarkable ductility improvement in Mg–Y alloys compared to pure Mg is caused by a high activity of pyramidal dislocations [5]. Their correct identification and the quantification of their contribution to the overall shear hence is the key to understand and describe the plastic behavior of these alloys. Analysis of the active dislocations and slip systems during early stage room temperature deformation (~3% engineering strain) of Mg–Y reveals

- high activity of pyramidal $\langle c+a \rangle$ dislocations gliding on 1st and 2nd order pyramidal planes;
- most pyramidal dislocations are screw dislocations;
- collinearly dissociated dislocations with $\langle c+a \rangle \rightarrow 1/2\langle c+a \rangle + 1/2\langle c+a \rangle$ are observed in the glide plane;
- frequent cross-slip of pyramidal dislocations is observed enabling the dislocations to cross-slip from one pyramidal plane to other pyramidal planes;
- prismatic $\langle a \rangle$ slip was not observed after 3% (engineering strain) deformation.

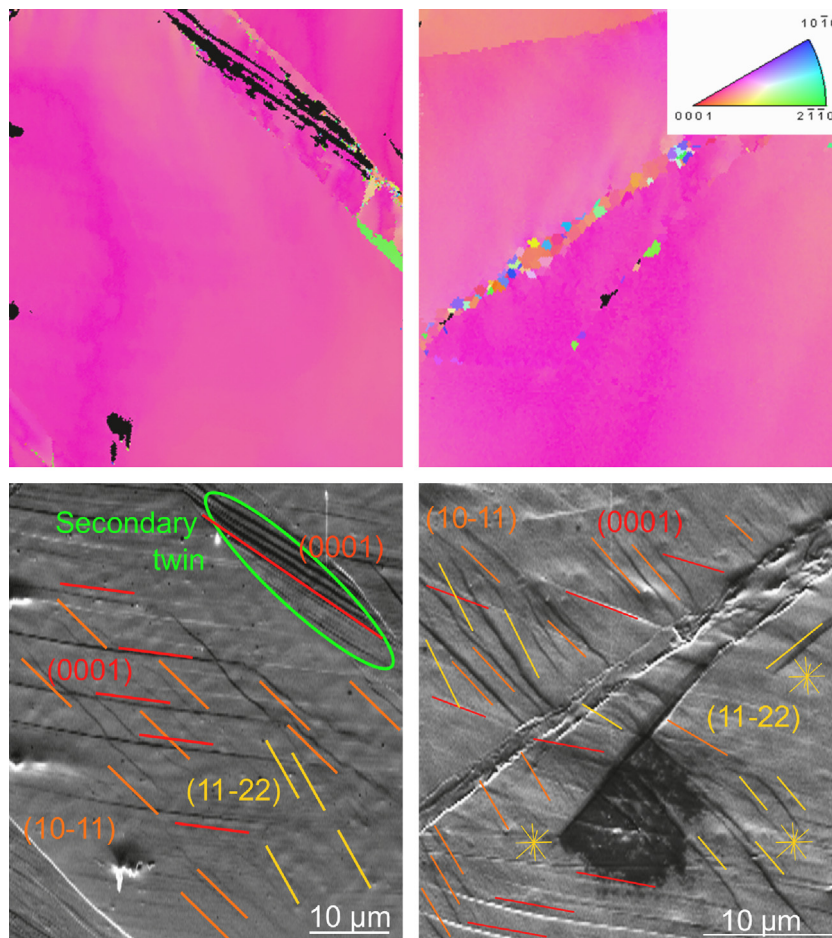


Fig. 5. SEM-EBSD based slip trace analysis and corresponding inverse pole figure maps on Mg–3Y: red lines show basal slip traces (0001); orange lines show 1st order pyramidal slip traces ($10\bar{1}1$); and yellow lines show 2nd order pyramidal slip traces ($11\bar{2}2$); the slip traces were identified using the software OIM. (For interpretation of the references to color in this figure legend, the reader is referred to the web version of this article.)

Acknowledgments

The authors are grateful to the Deutsche Forschungsgemeinschaft (DFG) for financial support through the project “Fundamental investigation of the mechanisms of deformation and recrystallization of cold deformable Mg alloys micro-alloyed with rare earth elements and microstructure optimization for the development of a new class of Mg-alloys”, Grant YI 103 1-2/ ZA 278 6-2.

References

- [1] S.R. Agnew, J.F. Nie, *Scr. Mater.* 63 (2010) 671–673.
- [2] S.L. Couling, J.F. Pashak, L. Sturkey, *Trans. ASM* 51 (1959) 94–107.
- [3] Y. Chino, M. Kado, M. Mabuchi, *Acta Mater.* 56 (2008) 387–394.
- [4] Y. Chino, M. Kado, M. Mabuchi, *Mater. Sci. Eng. A* 494 (1–2) (2008) 343–349.
- [5] S. Sandlöbes, S. Zaefferer, I. Schestakow, S. Yi, R. Gonzales-Martinez, *Acta Mater.* 59 (2) (2011) 429–439.
- [6] S. Sandlöbes, M. Friák, S. Zaefferer, A. Dick, S. Yi, D. Letzig, Z. Pei, L.-F. Zhu, J. Neugebauer, D. Raabe, *Acta Mater.* 60 (2012) 3011–3021.
- [7] M.R. Barnett, *Mater. Sci. Eng. A* 464 (2007) 1–7.
- [8] M.R. Barnett, *Mater. Sci. Eng. A* 464 (2007) 8–16.
- [9] I.J. Beyerlein, J. Wang, M.R. Barnett, C.N. Tome, *Proc. R. Soc. A* 468 (2012) 1496–1520.
- [10] N.J. Lane, S.I. Simak, A.S. Mikhaylushkin, I.A. Abrikosov, L. Hultman, M.W. Barsoum, *Phys. Rev. B* 84 (2011) 7184101 84 (2011) 7.
- [11] J.J. Jonas, S. Mu, T. Al-Samman, G. Gottstein, L. Jiang, E. Martin, *Acta Mater.* 59 (2011) 2046–2056.
- [12] M.H. Yoo, *Metall. Trans. A Phys. Metall. Mater. Sci.* 12 (1981) 409–418.
- [13] H. Yoshinaga, R. Horiuchi, *Trans. JIM* 4 (1963) 1–8.
- [14] H. Yoshinaga, R. Horiuchi, *Trans. JIM* 5 (1963) 14–21.
- [15] H. Miura, X. Yang, T. Sakai, H. Nogawa, S. Miura, Y. Watanabe, J. Jonas, *Phil. Mag.* 85 (30) (2005) 3553–3565.
- [16] P.B. Hirsch, J.S. Lally, *Phil. Mag.* 12 (117) (1965) 595–648.
- [17] S. Ando, H. Tonda, *Mater. Sci. Forum* 350–351 (2000) 43–48.
- [18] S. Ando, M. Tanaka, H. Tonda, *Mater. Sci. Forum* 419–422 (2003) 87–92.
- [19] A. Galiyev, R. Kaibyshev, G. Gottstein, *Acta Mater.* 49 (2001) 1199–1207.
- [20] S.R. Agnew, J.A. Horton, M.H. Yoo, *Metall. Mater. Trans. A* 33 (3) (2002) 851–858.
- [21] J. Koike, T. Kobayashi, T. Mukai, H. Watanabe, M. Suzuki, K. Maruyama, K. Higashi, *Acta Mater.* 51 (2003) 2055–2065.
- [22] Y. Chino, M. Kado, M. Mabuchi, *Mater. Sci. Eng. A* 494 (2008) 343–349.
- [23] F. Kang, J.Q. Liu, J.T. Wang, X. Zhao, *Scr. Mater.* 61 (2009) 844–847.
- [24] M.H. Liang, D.J. Bacon, *Phil. Mag. A* 53 (1986) 163–179.
- [25] M.H. Liang, D.J. Bacon, *Phil. Mag. A* 53 (1986) 181–204.
- [26] M.H. Liang, D.J. Bacon, *Phil. Mag. A* 53 (1986) 205–220.
- [27] S. Ando, T. Gotoh, H. Tonda, *Metall. Mater. Trans. A* 33 (3) (2002) 823–829.
- [28] Y. Minonishi, S. Ishioka, M. Koiwa, M. Morozumi, M. Yamaguchi, *Phil. Mag. A* 43 (1981) 1017–1026.
- [29] Y. Minonishi, S. Ishioka, M. Koiwa, M. Morozumi, M. Yamaguchi, *Phil. Mag. A* 44 (1981) 1225–1237.
- [30] Y. Minonishi, S. Ishioka, M. Koiwa, M. Morozumi, *Phil. Mag. A* 46 (1982) 761–770.
- [31] Y. Minonishi, S. Ishioka, M. Koiwa, M. Morozumi, M. Yamaguchi, *Phil. Mag. A* 45 (1982) 835–850.
- [32] H. Numakura, Y. Minonishi, M. Koiwa, *Phil. Mag. A* 62 (5) (1990) 525–543.
- [33] H. Numakura, Y. Minonishi, M. Koiwa, *Phil. Mag. A* 62 (5) (1990) 545–556.
- [34] J.R. Morris, K.M. Ho, K.Y. Chen, G. Rengarajan, M.H. Yoo, *Model. Simul. Mater. Sci. Eng.* 8 (2000) 25–35.
- [35] M.H. Yoo, J.R. Morris, K.M. Ho, S.R. Agnew, *Metall. Mater. Trans. A* 33 (2002) 813–822.
- [36] B. Li, E. Ma, *Acta Mater.* 57 (2009) 1734–1743.
- [37] B. Li, E. Ma, *Phil. Mag.* 89 (14) (2009) 1223–1235.
- [38] B. Li, P.F. Yan, M.L. Sui, E. Ma, *Acta Mater.* 58 (2010) 173–179.
- [39] H.S. Rosenbaum, *Deformation Twinning*, in: R.E. Reed-Hill, J.P. Hirth, H.C. Rogers (Eds.), Gordon & Breach, New York, NY, 1964, pp. 43–76.
- [40] T. Nogaret, W.A. Curtin, J.A. Yasi, L.G. Hector Jr., D.R. Trinkle, *Acta Mater.* 58 (2010) 4332–4343.
- [41] S. Zaefferer, *Adv. Imaging Electron. Phys.* 125 (2003) 355.
- [42] S. Zaefferer, *J. Appl. Cryst.* 33 (2000) 10–25.